MDPI

Article

Flow Rate-Driven Morphology Evolution of Chemical Vapor Deposited WS$_2$ at Varying Temperatures

Himal Pokhrel [ID]**, Sanjay Mishra and Shawn Pollard** *[ID]

Department of Physics and Materials Science, University of Memphis, Memphis, TN 38152, USA;
hpokhrel@memphis.edu (H.P.); srmishra@memphis.edu (S.M.)
* Correspondence: shawn.pollard@memphis.edu

Abstract: Due to its unique electronic and optical properties, tungsten disulfide (WS$_2$) is a promising material for various device applications. However, achieving an efficient and cost-effective method for synthesizing large-area uniform WS$_2$ is still challenging. In this work, we demonstrate the synthesis of few-layer WS$_2$ crystallites by NaCl-assisted low-pressure chemical vapor deposition and study the effect of temperature and the carrier gas flow rate on the morphology, structure, and optical properties of the as-grown WS$_2$ films. We observe transitions between regular triangular to strongly disordered structures with sizes up to 50 μm through temperature and carrier gas flow rate tuning. As-grown samples were characterized by Raman spectroscopy, scanning electron microscopy, and X-ray photoelectron spectroscopy. The result of this work provides a path toward the optimization of growth conditions for obtaining WS$_2$ with desired morphologies for various applications.

1. Introduction

Two-dimensional transition metal dichalcogenides (2D-TMDs) have garnered significant interest due to their remarkable electrical, optical, and chemical properties. Among various 2D-TMDs, WS$_2$ has demonstrated high carrier mobility [1], strong spin-orbit coupling [2–4], and strong light–matter interactions [5,6] which have led to its proposed use in a variety of optoelectronic devices [7]. Further, due to its direct band gap of ~2.1 eV in monolayer form and indirect band gap of ~1.3 eV in bulk form, as well as its high stability, it is one of the most studied TMDs [8–10]. Along with the layer-dependent band gap, it exhibits significant spin orbit-induced band splitting and spin valley coupling [11,12]. This material is a promising candidate for application in semiconductor devices such as transistors and solar cells [13–15]. Due to their range of potential applications, a wide range of work has focused on the ability to control the morphology of TMDs, including WS$_2$, with chemical vapor deposition (CVD) being the most widely studied synthesis method owing to its scalability, cost-effectiveness, and the wide range of methods available in which to transfer as-grown material to other substrates for incorporation into devices [16].

However, CVD is further complicated by the wide range of experimental parameters that influence growth, including temperature, precursor material quantities, carrier gas type and flow rate, growth time, the inclusion of promotor materials, and growth geometry, among others [17]. For example, the morphology may be tuned from triangular to hexagonal by controlling the relative transition metal and chalcogen termination growth rates, which may be influenced by modulating the availability of each respective gas phase precursor. Previous works have demonstrated this through the tuning of precursor quantities [18], temperature [19], source substrate distances [20,21], or even through the introduction of an Ar plasma during growth [22]. More recently, various works have focused on the growth of irregular 2D-TMDs, including fractal and dendritic growth. The transition from regular triangular or hexagonal structures is driven by competition between

attachment rates of atoms to nucleated structures, detachment, and boundary diffusion. In the model of diffusion-limited aggregation, fractal or dendritic growth occurs once the attachment rate is too rapid and newly attached adatoms cannot diffuse to low-energy sites. This may occur in growth regimes with limited diffusion rates, i.e., at low temperatures or with a high metal-to-chalcogen ratio [23]. Other works have shown the ability to tune growth from triangular to disordered via increasing precursor mass transfer by increasing carrier gas flow rates [20]. Due to the higher fraction of edge sites that are catalytically active for hydrogen evolution reaction in these disordered structures, these structures have been proposed for use in electrocatalysis [24,25]. Of interest in our work is the role of temperature and carrier gas flow rate on the morphology transformation of ultrathin WS_2 grown via halide-assisted LP-CVD [26].

The use of NaCl as a promotor material to enhance the growth of TMDs from solid source transition metal oxide precursors has been previously established owing to its ability to lower the evaporation temperature of transition metal oxides and form volatile intermediate products, which enhances the formation rates of TMDs from precursor compounds. Previously, we have demonstrated the ability to tune growth from triangular to dendritic WS_2 through varying the amount of a NaCl promotor during growth, which allows the metal flux to be modulated [27]. Precursor flux may be further controlled by various other means, including increasing the temperature and carrier gas flow rates. Specifically, increasing the temperature may result in increased generation of gas-phase WO_3 and other volatile precursors, as well as increased chemical reaction rates driving the decomposition of WO_3 and the formation of WS_2, while increasing flow rates has been previously shown to increase mass transfer due to the improved transport of precursors to the substrate region [20,28,29]. Here, we demonstrate the ability to generate highly disordered WS_2 flakes with sizes above 50 μm by tuning both flow rates and temperature during the low-pressure chemical vapor deposition (LP-CVD) growth of WS_2 with a fixed quantity of NaCl.

2. Materials and Methods

WS_2 crystals were grown on SiO_2/Si substrates with a 300 nm thick thermal oxide layer by LP-CVD in a single heating zone furnace. Prior to growth, the nominally 5 cm long, 1.9 cm wide substrates were cleaned through a series of 15 min ultrasonication steps in acetone, isopropanol, and de-ionized water, respectively. Sulfur and tungsten oxide powders were precursor materials, with NaCl as a promotor material. A total of 500 mg of sulfur (99.98% purity, Sigma-Aldrich, St. Louis, MO, USA), and a mixture of 50 mg of WO_3 (99.9% purity, Sigma-Aldrich) were placed in two different alumina combustion boats of 10 mm in height and 6 cm in length. Subsequently, 2.5 mg of NaCl (99.5% purity, Sigma-Aldrich) was mixed into the boat containing WO_3. The WO_3/NaCl mixture was placed near the leading edge of the boat. The boats were loaded in a quartz tube with an inner diameter of 44 mm, with the substrate was placed on top of the combustion boat containing the mixture of WO_3 and NaCl, with the leading edge of the substrate aligned with the center of the mixture. A schematic of the LPCVD set-up used for the growth of WS_2 films is shown in Figure 1a. The boat was placed in the central heating zone while the sulfur was placed at the edge of the heating zone to control the vapor flow and prevent the early evaporation of sulfur.

After reaching a base pressure of nominally 400 mTorr, the tube was purged with 500 SCCM of argon gas. The tube was then heated to 300 °C in 15 min and allowed to sit at 300 °C under Ar flow for 10 min. The temperature of the furnace was then increased to the growth temperature at the rate of 10 °C per minute. The growth of the sample was carried out at temperatures of 700 °C, 800 °C, and 900 °C for 15 min. During the growth, the temperature of the crucible containing sulfur was fixed at nominally 180 °C. At each temperature, the flow rate of Ar was chosen to be either 25, 50, or 75 SCCM, allowing for the role of both temperature and flow rate on the resultant morphology to be observed. Following growth, the sample was rapidly cooled down to room temperature. The temperature profile for growth at 900 °C is shown in Figure 1c and is similar for

all temperatures studied. The process pressure for growth at 25, 50, and 75 SCCM was approximately 1.2, 1.5, and 1.8 Torr, respectively.
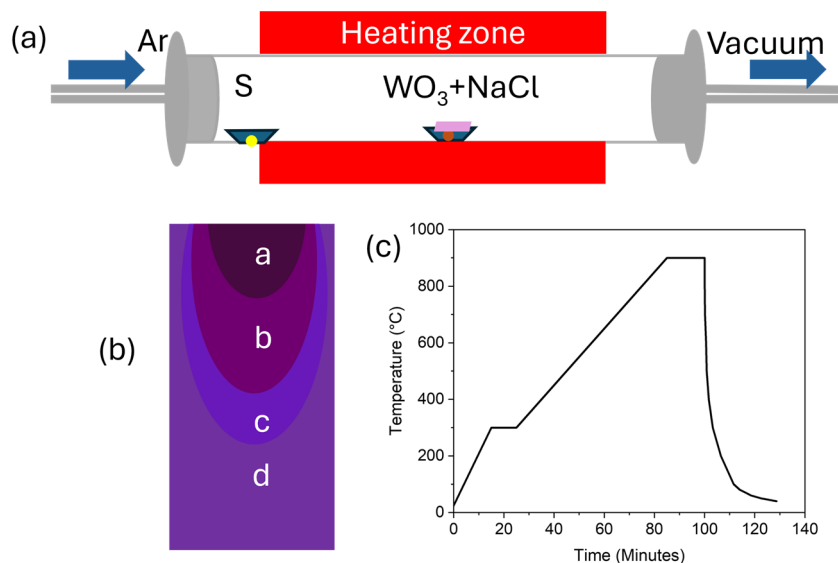

Figure 1. (**a**) Schematic of the CVD set-up and (**b**) a diagram depicting a typical zonal growth pattern, with different regions (a–d) corresponding to bulk, large flakes, transitioning to smaller, isolated growth, and no growth regions, respectively. (**c**) The temperature profile used during heating, growth, and cooling.

Following growth, the sample's chemical composition was examined by X-ray photoemission spectroscopy (XPS) using a Thermo Scientific (Waltham, MA, USA) K-Alpha XPS system with a 0.1 eV step size. The presence of WS_2 was also confirmed by Raman spectroscopy in a standard backscattering geometry and a 50x objective at room temperature using a Thermo Scientific DXR Raman Microscope with a 532 nm laser. An 1800 line/mm grating and a 50 μm slit aperture were used. Measurements were carried out near the region's center at various distances from the upstream edge of the substrate. Raman data were smoothed using a Savitzky–Golay filter. The variation in the morphology was studied using a Hitachi-4700 (Tokyo, Japan) field emission scanning electron microscope (FESEM) at an accelerating voltage of 10 kV and an emission current of 10 μA.

3. Results

Figure 2 shows the typical zonal growth pattern [30,31] for samples grown under varying temperatures and flow rates. Increasing the temperature or the flow rate leads to a more extensive growth region, as expected. Along the leading edge of the substrate, which is close to the WO_3 precursor, we observe mostly bulk growth, with growth transitioning to thin, isolated crystals, with size and density decreasing further from the leading edge. The extent of the growth and width of each region grows with both increasing temperature and flow rate, which is expected due to the increased precursor quantity and reaction rates resulting from both.
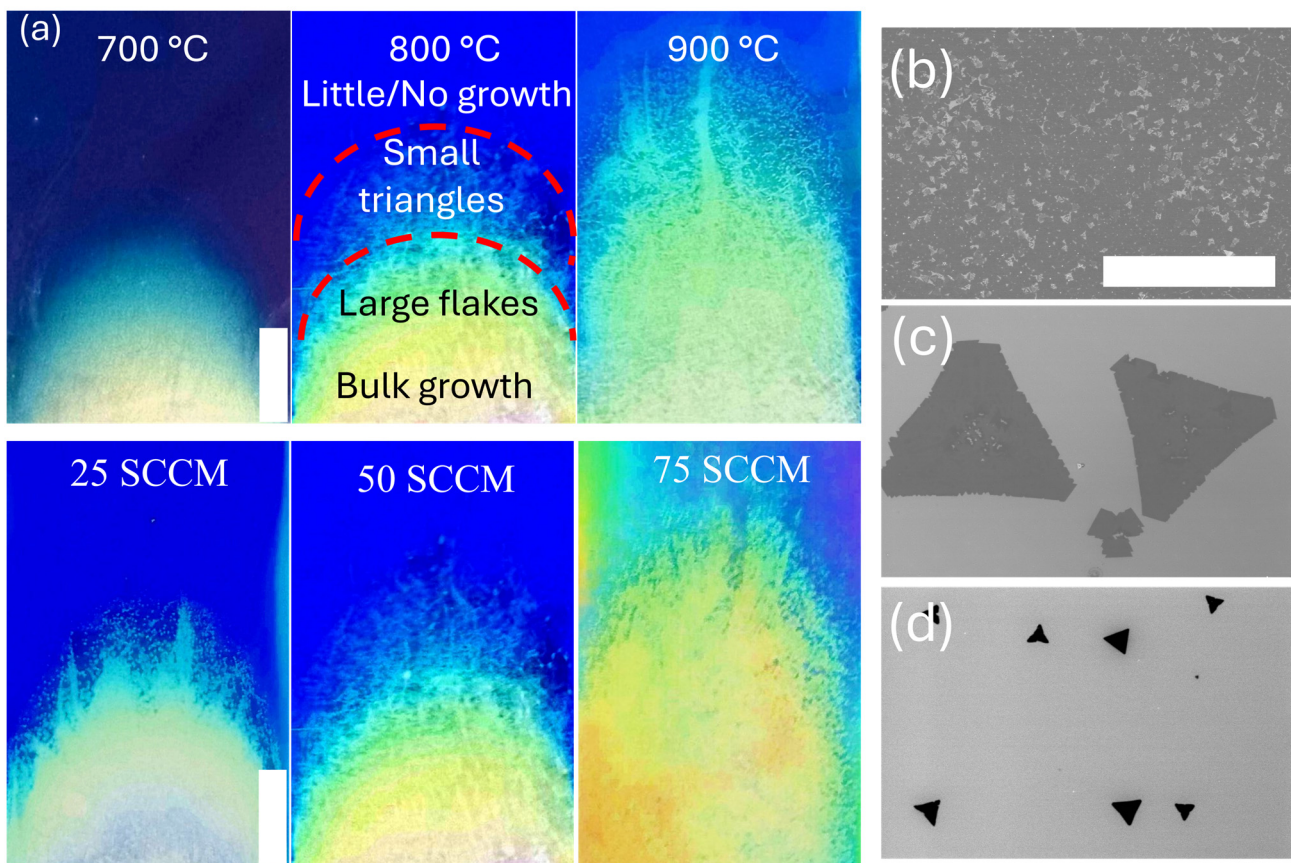
Figure 2. (**a**) Optical images showing the zonal growth pattern and relative extent of growth for (**top**) varying temperatures at a flow rate of 50 SCCM and (**bottom**) at varying flow rates at 800 °C, and representative SEM images in the region of (**b**) 0–1 cm, (**c**) 1–2 cm, and (**d**) 2–3 cm along the midpoint of the growth zone. The scale bar is 1 cm for (**a**) and 100 μm for (**b**–**d**).

Raman spectroscopy, shown in Figure 3, confirmed that this growth corresponds to WS_2. Raman measurements were taken in the central region 2 cm downstream from the leading edge of the substrate, as shown in Figure 4. Three primary peaks were observed for all samples at nominally 323, 352, and 420 cm^{-1}, in good agreement with that of mechanically exfoliated WS_2 and suggesting a lack of significant doping of halide or alkali metal atoms [26]. The peak at 352 cm^{-1} is a convolution of the in-plane vibrational E^1_{2g} mode and a second-order mode of the longitudinal acoustic phonon 2LA(M) peak. The peak near 420 cm^{-1} corresponds to the out-of-plane vibrational A_{1g} mode, while the peak around 323 cm^{-1} has been previously reported to result from a 2LA(M)-E^2_{2g} hybrid mode [32,33]. As the peak separation between E^1_{2g} and A_{1g} increases with increasing layer number, the difference between these peaks from sample to sample may be used to identify increased growth thickness [34]. At a fixed temperature of 800 °C, the peak separation changes from 67.2 cm^{-1} at 25 SCCM to 68.2 cm^{-1} at 50 SCCM and 68.9 cm^{-1} at 75 SCCM, indicating that increased flow rates resulted in thicker growth at equal distances downstream, which is consistent with the greater growth observed in optical images shown in Figure 2a. Further, increasing flow rates results in an increasing A_{1g}/E^1_{2g} intensity ratio, which is also associated with increasing growth at a given downstream distance. Similarly, peak separations of 66.3, 68.3, and 69.6 cm^{-1} were found for growth at a constant 50 SCCM flow rate and temperatures of 700, 800, and 900 °C, respectively, consistent with expected increasing thicknesses at a fixed position for increasing temperatures. For all samples, Raman spectra indicate growths of between 1 and 4 layers [11].
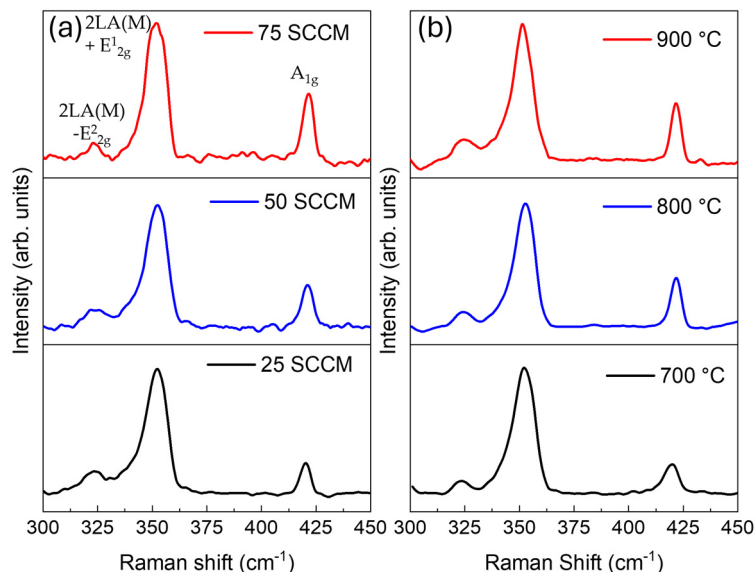
Figure 3. Raman spectra for samples grown at (**a**) 800 °C and varying flow rates, and (**b**) varying temperatures and a fixed 50 SCCM flow rate. Measurements were taken 2 cm from the leading edge of the substrate. Note that measurements taken at 50 SCCM were taken from different samples. However, this does not result in changes to the Raman spectra. Raman modes are marked in (**a**).

SEM images at 25 SCCM are shown in Figure 4a, with representative images taken at given substrate locations for varying flow rates to understand changes in morphology driven by flow rate and temperature. The total growth region increases as the temperature increases, with more growth downstream. At 700 °C, thin triangular crystals are observed both at the substrate leading edge and 1 cm downstream. Increasing temperatures lead to growth up to 4 cm and also drastic morphology changes, which are especially apparent at 900 °C, wherein the triangular structure becomes disordered, with similar structures referred to as dendritic, fractal, or semi-compact growth in previous works [24,25,27,35,36]. However, increasing the downstream distance decreases the overall structure size while the ordered triangular crystal structure is recovered. This recovery of triangular growth occurs at greater distances for increased temperatures or flow rates. At 50 SCCM, a similar transition is apparent, as shown in Figure 4b. However, the disordered transition occurs at the lower temperature of 800 °C, with a significantly larger disorder apparent at 900 °C and disordered growth extending further downstream. At 75 SCCM, as shown in Figure 4c, disordered growth appears even at 700 °C, and the disordered region at higher temperatures extends to even more distant regions of the substrate. It is apparent that both increased flow rate and temperature significantly enhance this transition to disordered growth. However, all structures retain a semi-compact triangular form. Even at the lowest temperatures, increasing flow rates result in disordered edges. For all samples, increasing the distance from the source results in lower density growth and the decreased size of individual elements, as expected owing to the gradient in metal precursor availability further from the substrate leading edge.

XPS measurements, shown in Figure 5, were taken 1 cm downstream from samples grown at 800 °C and 25 and 75 SCCM flow rates. Survey spectra indicate only small amounts of NaCl are present following growth, as indicated by the barely noticeable Na 1s peak. W 4f and S 2p signals are shown in Figure 5b,c, with fitting to Voigt profiles for each peak performed using the method described in [37]. The W 4f signal is comprised of W $4f_{5/2}$ and W $4f_{7/2}$ doublets belonging to W^{6+} and W^{4+} oxidation states, as well as a contribution from the W $5p_{3/2}$ state at a slightly higher binding energy. Fits assumed an area ratio between corresponding doublets of 4:3 per the multiplicity of corresponding levels, as well as equal line widths. The W^{4+} peaks are centered at binding energies of 35.1 and 33.0 eV for W $4f_{5/2}$ and W $4f_{7/2}$, respectively, which are characteristic of WS_2, with no

noticeable shift for both samples. Additional peaks corresponding to W^{6+}, characteristic of WO_3, are found at 37.8 and 35.9 eV. Binding energies for the S 2p doublet corresponding to S $2p_{1/2}$ and S $2p_{3/2}$ states are found at 163.8 and 162.5 eV for both samples. As no significant differences in intensity ratios or peak locations for W^{4+} and W^{6+} species are observed between samples, the transformation is not associated with changes to the local chemical environment and instead is related to the kinetics of crystal growth of similar species at the surface.
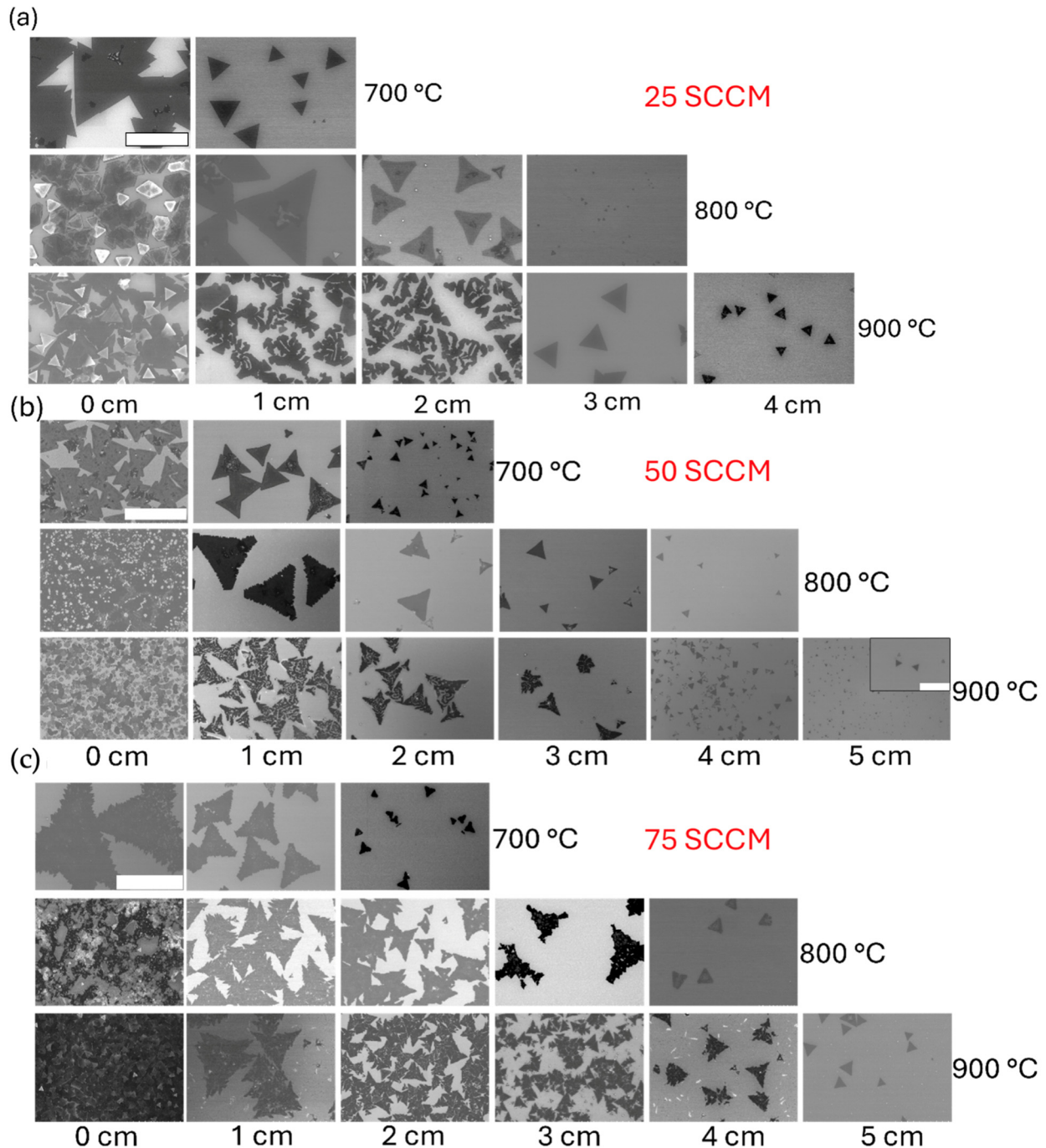

Figure 4. SEM images at various distances along the leading edge of the substrate for varying temperatures at a constant flow rate of (**a**) 25 SCCM, (**b**) 50 SCCM, and (**c**) 75 SCCM. The scale bar is 10 μm for all images in (**a**) and 100 μm in (**b**) and (**c**). The magnified image on the inset (**b**) has a scale bar of 10 μm and indicates small-scale triangular growth.
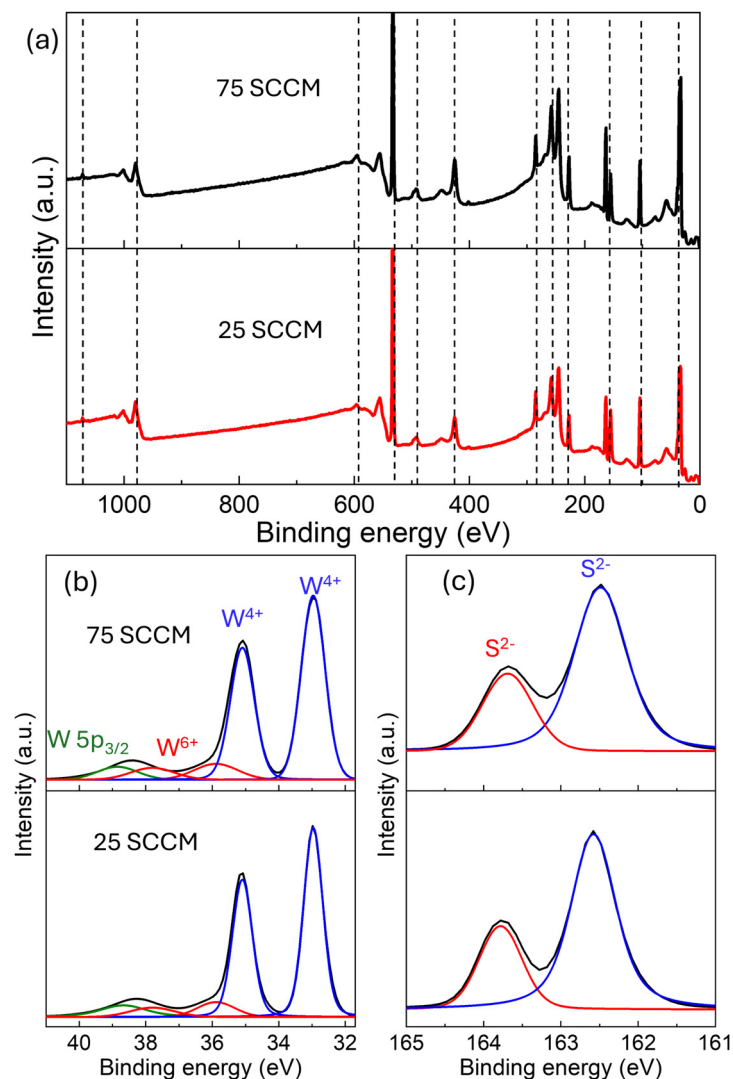
Figure 5. XPS spectra correspond with samples grown at 800 °C and the indicated flow rates. (**a**) Survey spectra showing the Na 1s, O KLL, W 4s, O 1s, W $4P_{1/2}$, W $4p_{3/2}$, C 1s, W 4d, S 2s, S 2p, Si 2p, and W 4f states in the order of decreasing binding energy. (**b**,**c**) show high-resolution scans corresponding to the W 4f and S2p states. The different rows in (**b**) and (**c**) represent flow rates indicated in (**b**).

4. Discussion

The transition from regular triangular to dendritic growth is explained by the competition between attachment rates to the nucleated structures, detachment, and edge diffusion rates. Adatoms can diffuse along the edge for slow growth to form the most stable configuration, resulting in compact domains. However, if the attachment rate is too high or the diffusion rate too low, adatoms can no longer sufficiently diffuse to the lowest energy sites [25,35,38,39]. Kinetic Monte Carlo (KMC) studies have shown that the degree of edge disorder and transition to dendritic growth at a given temperature is then related to the total flux and flux ratio of chalcogen and transition metals (C/M ratio) [36]. For example, at a low metal flux, growth was shown to produce compact triangles with no sensitivity to the C/M ratio. However, increasing the metal flux while maintaining a low C/M ratio leads to the growth of semi-compact, disordered triangular structures similar to those observed in our works. It is clear that increasing temperature at the growth site and the WO$_3$/NaCl mixture will result in an increased metal flux while maintaining the same flux of S to the substrate and, therefore, can drive the transition from triangular to semi-compact structures seen in this work, as this will result in maintaining a low C/M ratio while enhancing the metal

flux. Similarly, the recovery of triangular growth further downstream may be explained by decreasing tungsten precursor concentrations with distance from the source material. The role of flow rate is somewhat more complex. Increasing flow rates can enhance the mass transfer process, transforming growth from thermodynamic to kinetic [20]. While both chalcogen and metal flux increase in this scenario, the ratio may not significantly change. As a result, flux may play a similar role to temperature in determining the morphology through primarily modulating the metal flux while having a lesser effect on the C/M ratio. This is further supported by the observation of a transition from straight to curved-edge triangular growth, as shown in Figure 6, wherein this describes how well the edge conforms to a straight line connecting triangle vertices. For all semi-compact domains, a curve away from a straight line is clearly visible, which reverses midway through the given edge. This structure has been reported previously to result from an imbalance of the C/M ratio and can be driven by either too high measures of chalcogen or metal fluxes [20]. The recovery of the straight edge with increasing distance downstream indicates that this is the result of a C/M ratio that is too low, wherein the ratio increases further downstream. Similar deviations from straight-line edges were also demonstrated for semi-compact growth in KMC models [36].
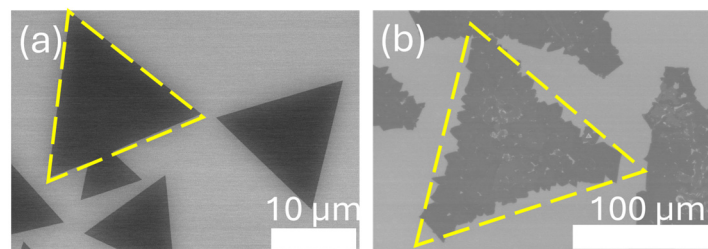

Figure 6. SEM images show the emergence of deviations from straight-edge triangular growth as the flow rate is increased from (**a**) 25 SCCM to (**b**) 75 SCCM. Otherwise, images are taken under identical growth conditions at 700 °C and 1 cm downstream.

5. Conclusions

We have grown WS$_2$ crystals with low-pressure CVD on thermally oxidized Si substrates. We observe a transition from small, smooth triangles to large, semi-compact growth with zagged edges by systematically varying the temperature and carrier gas flow rate. The physical and chemical properties of synthesized samples have been analyzed with the help of optical microscopy, Raman spectroscopy, X-ray photoelectron spectroscopy (XPS), and SEM. In line with previous reports, increasing metal flux and decreasing the C/M ratio transforms a sample from traditional compact triangular growth to more complex, semi-compact growth with significant disorder while maintaining a roughly triangular structure. Temperature enhances metal flux via the increased evaporation and decomposition of the WO$_3$ precursor itself. Meanwhile, flow rate modifications play a similar, albeit more complicated, role by enhancing both metal and sulfur flux. However, our results indicate that metal flux enhancements play a dominant role, resulting in changes in morphology similar to those caused by enhancing temperature. The ability to control the morphology of the 2D-TMDC by controlling the process parameters has important applications in optoelectronics and electrochemistry, allowing for the enhancement or suppression of disorder while also allowing for the tunability of the number of active edge sites.

Author Contributions: Conceptualization, H.P. and S.P.; methodology, H.P. and S.P.; formal analysis, H.P., S.P. and S.M.; investigation, H.P.; resources, S.P and S.M.; data curation, H.P.; writing—original draft preparation, S.P. and H.P.; writing—review and editing, H.P., S.P. and S.M.; visualization, H.P. and S.P.; supervision, S.P.; project administration, S.P. All authors have read and agreed to the published version of the manuscript.

References

1. Ovchinnikov, D.; Allain, A.; Huang, Y.-S.; Dumcenco, D.; Kis, A. Electrical Transport Properties of Single-Layer WS$_2$. *ACS Nano* **2014**, *8*, 8174–8181. [CrossRef]
2. Shi, S.; Liang, S.; Zhu, Z.; Cai, K.; Pollard, S.D.; Wang, Y.; Wang, J.; Wang, Q.; He, P.; Yu, J.; et al. All-electric magnetization switching and Dzyaloshinskii-Moriya interaction in WTe2/ferromagnet heterostructures. *Nat. Nanotechnol.* **2019**, *14*, 945–949. [CrossRef]
3. Xiao, D.; Liu, G.-B.; Feng, W.; Xu, X.; Yao, W. Coupled Spin and Valley Physics in Monolayers of MoS 2 and and Other Group-VI Dichalcogenides. *Phys. Rev. Lett.* **2012**, *108*, 196802. [CrossRef]
4. Zhu, Z.Y.; Cheng, Y.C.; Schwingenschlögl, U. Giant spin-orbit-induced spin splitting in two-dimensional transition-metal dichalcogenide semiconductors. *Phys. Rev. B* **2011**, *84*, 153402. [CrossRef]
5. Wurstbauer, U.; Miller, B.; Parzinger, E.; Holleitner, A.W. Light–matter interaction in transition metal dichalcogenides and their heterostructures. *J. Phys. D Appl. Phys.* **2017**, *50*, 173001. [CrossRef]
6. Cao, J.; Fiore, S.; Klinkert, C.; Vetsch, N.; Luisier, M. Light-matter interactions in van der Waals photodiodes from first principles. *Phys. Rev. B* **2022**, *106*, 035306. [CrossRef]
7. Wang, Q.H.; Kalantar-Zadeh, K.; Kis, A.; Coleman, J.N.; Strano, M.S. Electronics and optoelectronics of two-dimensional transition metal dichalcogenides. *Nat. Nanotechnol.* **2012**, *7*, 699–712. [CrossRef]
8. Zhao, W.; Ghorannevis, Z.; Chu, L.; Toh, M.; Kloc, C.; Tan, P.-H.; Eda, G. Evolution of Electronic Structure in Atomically Thin Sheets of WS$_2$ and WSe$_2$. *ACS Nano* **2013**, *7*, 791–797. [CrossRef]
9. Braga, D.; Lezama, I.G.; Berger, H.; Morpurgo, A.F. Quantitative Determination of the Band Gap of WS$_2$ with Ambipolar Ionic Liquid-Gated Transistors. *Nano Lett.* **2012**, *12*, 5218–5223. [CrossRef]
10. Voiry, D.; Mohite, A.; Chhowalla, M. Phase engineering of transition metal dichalcogenides. *Chem. Soc. Rev.* **2015**, *44*, 2702–2712. [CrossRef]
11. Zeng, H.; Liu, G.-B.; Dai, J.; Yan, Y.; Zhu, B.; He, R.; Xie, L.; Xu, S.; Chen, X.; Yao, W.; et al. Optical signature of symmetry variations and spin-valley coupling in atomically thin tungsten dichalcogenides. *Sci. Rep.* **2013**, *3*, 1608. [CrossRef]
12. Nayak, P.K.; Lin, F.-C.; Yeh, C.-H.; Huang, J.-S.; Chiu, P.-W. Robust room temperature valley polarization in monolayer and bilayer WS$_2$. *Nanoscale* **2016**, *8*, 6035–6042. [CrossRef]
13. Hwang, W.S.; Remskar, M.; Yan, R.; Protasenko, V.; Tahy, K.; Chae, S.D.; Zhao, P.; Konar, A.; Xing, H.; Seabaugh, A.; et al. Transistors with chemically synthesized layered semiconductor WS$_2$ exhibiting 105 room temperature modulation and ambipolar behavior. *Appl. Phys. Lett.* **2012**, *101*, 013107. [CrossRef]
14. Iqbal, M.W.; Iqbal, M.Z.; Khan, M.F.; Shehzad, M.A.; Seo, Y.; Park, J.H.; Hwang, C.; Eom, J. High-mobility and air-stable single-layer WS$_2$ field-effect transistors sandwiched between chemical vapor deposition-grown hexagonal BN films. *Sci. Rep.* **2015**, *5*, 10699. [CrossRef]
15. Bin Rafiq, K.S.; Amin, N.; Alharbi, H.F.; Luqman, M.; Ayob, A.; Alharthi, Y.S.; Alharthi, N.H.; Bais, B.; Akhtaruzzaman, M. WS$_2$: A New Window Layer Material for Solar Cell Application. *Sci. Rep.* **2020**, *10*, 771. [CrossRef]
16. Schranghamer, T.F.; Sharma, M.; Singh, R.; Das, S. Review and comparison of layer transfer methods for two-dimensional materials for emerging applications. *Chem. Soc. Rev.* **2021**, *50*, 11032–11054. [CrossRef]
17. Kang, T.; Tang, T.W.; Pan, B.; Liu, H.; Zhang, K.; Luo, Z. Strategies for Controlled Growth of Transition Metal Dichalcogenides by Chemical Vapor Deposition for Integrated Electronics. *ACS Mater. Au* **2022**, *2*, 665–685. [CrossRef]
18. Hussain, S.; Xu, R.; Xu, K.; Lei, L.; Meng, L.; Zheng, Z.; Xing, S.; Guo, J.; Dong, H.; Liaqat, A.; et al. Strain-induced hierarchical ripples in MoS2 layers investigated by atomic force microscopy. *Appl. Phys. Lett.* **2020**, *117*, 153102. [CrossRef]
19. Chen, F.; Su, W.; Zhao, S.; Lv, Y.; Ding, S.; Fu, L. Morphological evolution of atomically thin MoS$_2$ flakes synthesized by a chemical vapor deposition strategy. *CrystEngComm* **2020**, *22*, 4174–4179. [CrossRef]
20. Wang, S.; Rong, Y.; Fan, Y.; Pacios, M.; Bhaskaran, H.; He, K.; Warner, J.H. Shape Evolution of Monolayer MoS$_2$ Crystals Grown by Chemical Vapor Deposition. *Chem. Mater.* **2014**, *26*, 6371–6379. [CrossRef]
21. Saenz, G.A.L.; Biswas, C.; Yamaguchi, H.; Villarrubia, C.N.; Mohite, A.D.; Kaul, A.B. Effects of Synthesis Parameters on CVD Molybdenum Disulfide Growth. *MRS Adv.* **2016**, *1*, 2291–2296. [CrossRef]
22. Pokhrel, H.; Duncan, J.J.A.; Woli, Y.B.; Hoang, T.B.; Pollard, S.D. The effect of Ar plasma on the space-confined growth of MoS$_2$ with low-pressure chemical vapor deposition. *AIP Adv.* **2023**, *13*, 065322. [CrossRef]
23. Wu, L.; Yang, W.; Wang, G. Mechanism of substrate-induced anisotropic growth of monolayer WS$_2$ by kinetic Monte Carlo simulations. *NPJ 2D Mater. Appl.* **2019**, *3*, 6. [CrossRef]

24. Xu, W.; Li, S.; Zhou, S.; Lee, J.K.; Wang, S.; Sarwat, S.G.; Wang, X.; Bhaskaran, H.; Pasta, M.; Warner, J.H. Large Dendritic Monolayer MoS$_2$ Grown by Atmospheric Pressure Chemical Vapor Deposition for Electrocatalysis. *ACS Appl. Mater. Interfaces* **2018**, *10*, 4630–4639. [CrossRef]

25. Ma, J.; Li, X.; Gan, L.; Zhang, S.; Cao, Y.; Nie, Z.; Wang, X.; Ma, D.; He, L.; Nie, J.; et al. Controlling the dendritic structure and the photo-electrocatalytic properties of highly crystalline MoS$_2$ on sapphire substrate. *2D Mater.* **2018**, *5*, 031015. [CrossRef]

26. Li, S.; Wang, S.; Tang, D.-M.; Zhao, W.; Xu, H.; Chu, L.; Bando, Y.; Golberg, D.; Eda, G. Halide-assisted atmospheric pressure growth of large WSe$_2$ and WS$_2$ monolayer crystals. *Appl. Mater. Today* **2015**, *1*, 60–66. [CrossRef]

27. Pokhrel, H.; Duncan, J.J.A.; Krause, B.; Hoang, T.B.; Pollard, S.D. Transformation from dendritic to triangular growth of WS$_2$ via NaCl assisted low-pressure chemical vapor deposition. *J. Vac. Sci. Technol. A* **2024**, *42*, 042203. [CrossRef]

28. Di, X.; Wang, F.; Wei, J.; Shen, J.; Zhang, B.; Shan, X.; Lin, X.; Hao, Y.; Zhang, K. Controlled synthesis of WS$_2$ with different layers by tuning flow rates. *Mater. Sci. Eng. B* **2020**, *261*, 114756. [CrossRef]

29. Lin, X.; Liu, Y.; Wang, K.; Wei, C.; Zhang, W.; Yan, Y.; Li, Y.J.; Yao, J.; Zhao, Y.S. Two-Dimensional Pyramid-like WS$_2$ Layered Structures for Highly Efficient Edge Second-Harmonic Generation. *ACS Nano* **2018**, *12*, 689–696. [CrossRef]

30. Somphonsane, R.; Chiawchan, T.; Bootsa-Ard, W.; Ramamoorthy, H. CVD Synthesis of MoS$_2$ Using a Direct MoO$_2$ Precursor: A Study on the Effects of Growth Temperature on Precursor Diffusion and Morphology Evolutions. *Materials* **2023**, *16*, 4817. [CrossRef]

31. Chiawchan, T.; Ramamoorthy, H.; Buapan, K.; Somphonsane, R. CVD Synthesis of Intermediate State-Free, Large-Area and Continuous MoS$_2$ via Single-Step Vapor-Phase Sulfurization of MoO$_2$ Precursor. *Nanomaterials* **2021**, *11*, 2642. [CrossRef]

32. Chen, Y. Growth of a Large, Single-Crystalline WS$_2$ Monolayer for High-Performance Photodetectors by Chemical Vapor Deposition. *Micromachines* **2021**, *12*, 137. [CrossRef]

33. Lee, Y.-H.; Yu, L.; Wang, H.; Fang, W.; Ling, X.; Shi, Y.; Lin, C.-T.; Huang, J.-K.; Chang, M.-T.; Chang, C.-S.; et al. Synthesis and Transfer of Single-Layer Transition Metal Disulfides on Diverse Surfaces. *Nano Lett.* **2013**, *13*, 1852–1857. [CrossRef]

34. Berkdemir, A.; Gutiérrez, H.R.; Botello-Méndez, A.R.; Perea-López, N.; Elías, A.L.; Chia, C.-I.; Wang, B.; Crespi, V.H.; López-Urías, F.; Charlier, J.-C.; et al. Identification of individual and few layers of WS$_2$ using Raman Spectroscopy. *Sci. Rep.* **2013**, *3*, 1755. [CrossRef]

35. Chowdhury, S.; Roy, A.; Bodemann, I.; Banerjee, S.K. Two-Dimensional to Three-Dimensional Growth of Transition Metal Diselenides by Chemical Vapor Deposition: Interplay between Fractal, Dendritic, and Compact Morphologies. *ACS Appl. Mater. Interfaces* **2020**, *12*, 15885–15892. [CrossRef]

36. Nie, Y.; Liang, C.; Zhang, K.; Zhao, R.; Eichfeld, S.M.; Cha, P.-R.; Colombo, L.; A Robinson, J.; Wallace, R.M.; Cho, K. First principles kinetic Monte Carlo study on the growth patterns of WSe$_2$ monolayer. *2D Mater.* **2016**, *3*, 025029. [CrossRef]

37. Chen, P.; Baldwin, M.; Bandaru, P.R. Hierarchically structured, oxygen deficient, tungsten oxide morphologies for enhanced photoelectrochemical charge transfer and stability. *J. Mater. Chem. A* **2017**, *5*, 14898–14905. [CrossRef]

38. Chen, S.; Gao, J.; Srinivasan, B.M.; Zhang, G.; Sorkin, V.; Hariharaputran, R.; Zhang, Y.-W. Origin of ultrafast growth of monolayer WSe$_2$ via chemical vapor deposition. *npj Comput. Mater.* **2019**, *5*, 28. [CrossRef]

39. Nie, Y.; Liang, C.; Cha, P.-R.; Colombo, L.; Wallace, R.M.; Cho, K. A kinetic Monte Carlo simulation method of van der Waals epitaxy for atomistic nucleation-growth processes of transition metal dichalcogenides. *Sci. Rep.* **2017**, *7*, 2977. [CrossRef]